Aircraft Wake-Vortex Decay in Ground Proximity—Physical Mechanisms and Artificial Enhancement

Anton Stephan,* Frank Holzäpfel,† and Takashi Misaka‡
DLR, German Aerospace Research Center, 82234 Oberpfaffenhofen, Germany

DOI: 10.2514/1.C032179

Aircraft wake-vortex evolution in ground proximity is investigated numerically by means of large-eddy simulations. The simulations are performed either with a flat ground or with different modifications to the ground surface to trigger rapid vortex decay. The impact of environmental turbulence in terms of turbulent wind is taken into account, where wall-resolved and wall-modeled large-eddy simulation are performed for low- and high-Reynolds-number cases, respectively. To understand wake-vortex decay mechanisms in ground proximity, the interaction of primary and secondary vortices is carefully investigated. We find that vortex decay can be initiated at an earlier time and substantially accelerated with obstacles at the ground. We explain the fundamental vortex dynamics describing five characteristics of the phenomenon and quantify the decay. We demonstrate that similar effects can be achieved, employing relatively small plate lines as opposed to the original large block-shaped barriers. The obstacles trigger two kinds of so-called end effects: pressure disturbances propagating within the vortex cores and secondary vortex structures propagating along the outside of the vortex cores.

I. Introduction

AS A consequence of lift generation by aircraft wings of finite span, vortex sheets shed off the wings, roll up, and form a pair of counter-rotating vortices. The evolving two-vortex system persists for a long period of time, possessing a high amount of kinetic energy and thereby posing a potential hazard to following aircraft. To mitigate wake-vortex encounter risk, regulatory separation distances between aircraft weight classes have to be met, which limit the possible handling capacity of an airport. Therefore, the investigation of wake-vortex behavior and decay is an important issue for commercial aviation [1–3].

The probability of encountering wake vortices increases significantly during final approach in ground proximity because rebounding vortices may not leave the flight corridor vertically. Moreover, the advection by weak crosswinds may compensate the self-induced lateral vortex transport. Therefore, the clearance of the flight corridor by descent and advection of the vortices is strongly restricted. Because of the low height of the aircraft above the ground, the possibility of the pilot being able to counteract the imposed rolling moment is restricted [4,5]. Reliable wake-vortex prediction in ground proximity is crucial for a wake-vortex advisory system (WVAS). This is why the evolution of wake vortices close to the ground has received much attention during the last decades [4,6,7].

The evolution of a wake-vortex system in ground proximity results in a complex three-dimensional flow. When counter-rotating vortices approach a flat surface or are generated at low altitude, they diverge. An outboard directed flow is induced by the vortices on the surface and vorticity of opposite sign is produced in a boundary layer [8]. The induced flow near the surface experiences an adverse pressure gradient, which is strong enough to cause flow separation, leading to the formation of a separation bubble at the ground. Flow simulations have shown how pairs of secondary vortices are produced from the separation region and then detach and interact with the primary vortices [9–11]. The presence of an ambient crosswind induces another boundary layer corresponding to a vorticity layer at the ground. In contrast to considerations without crosswind, this causes an asymmetric situation. The sudden eruption of wake-vortex induced wall vorticity is faster and more intense for the downwind vortex where the crosswind shear-generated vorticity and the secondary vorticity have the same sign but is attenuated for the upwind vortex. There have been numerous attempts to accelerate vortex decay deliberately out of ground proximity, one example of which is described in [12]. However, much less work has been done for acceleration of wake-vortex decay in ground proximity.

The interaction of a counter-rotating two-vortex system with a flat surface using numerical simulations has been investigated so far with different approaches, which either resolve or model the wall. Wall-resolved direct numerical simulations (DNSs) [13] or large-eddy simulations (LESs) have been employed [14]. The resolution requirements for the boundary-layer flow limit the Reynolds number not only in DNS but also in LES. In LES, the subgrid-scale model only works properly, if the modeled part of the flow contributes to a relatively small extent to the turbulent kinetic energy (TKE). Close to walls, small structures mainly account for the TKE such that the resolution close to walls has to be refined in LES as well as in DNS. Up to now, values of $Re_\Gamma = \Gamma/\nu$ on the order of 20,000 have been realized for wall-resolved LES for vortex flow [14]. This approach allows the investigation of coherent structures close to the wall at the expense of a relatively low Re_Γ.

Another possibility is to use wall-modeling functions [15], which allows considering realistic Reynolds numbers of up to 10^7. However, this approach does not resolve the turbulent structures generated at the ground. Similar to [14], we conduct wall-resolved LES at a Reynolds number of $Re_\Gamma = 23,130$. Further, we discuss the effect of a wall model in connection with higher Reynolds numbers, too.

In this paper, we analyze how coherent structures generated in turbulent boundary layers advance wake-vortex decay. With this knowledge, we suggest a new method to accelerate vortex decay, exploiting fundamental properties of vortex dynamics. Vortex decay can be initiated locally and accelerated globally with dedicated obstacles installed at the ground. To put it simply, we find that the obstacle causes the flow to redirect the force that normally causes the wake vortices to rebound into early turbulent vortex decay. This means that the secondary vortices interact more rapidly with the primary vortices. We describe this effect qualitatively and determine quantitatively to what extent wake-vortex decay can be accelerated. It turns out that the design and arrangement of the obstacles can be

Presented as Paper 2012-2672 at the 4th AIAA Atmospheric and Space Environments Conference, 2012, New Orleans, 25–28 June 2012; received 24 October 2012; revision received 5 February 2013; accepted for publication 8 February 2013; published online 19 June 2013.

*Graduate Student, Institute for Atmospheric Physics; Anton.Stephan@dlr.de.

†Senior Research Scientist, Institute for Atmospheric Physics.

‡Research Scientist, Institute for Atmospheric Physics.

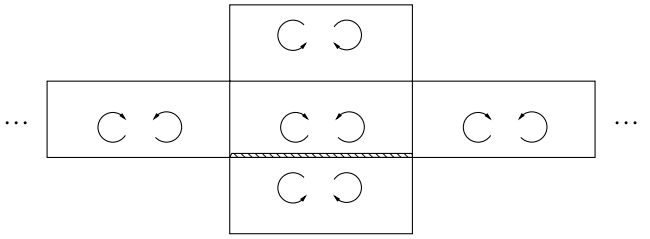

Fig. 1 Schematic of the wake-vortex initialization employing mirror and image vortices.

optimized. The suggested ground-based and passive method should require relatively small technical effort to be tested and be introduced at airports. A respective patent entitled "Surface Structure on a Ground Surface for Accelerating Decay of Wake Turbulence in the Short Final of an Approach to a Runway" has been filed under number DE 10 2011 010 147.

The obstacles trigger two kinds of disturbances that may both be considered as end effects [16] traveling along the primary vortices. One end effect is caused by an increase of pressure, propagating along the vortex core, and another one stems from the roll-up of secondary vorticity at the obstacle edges propagating along the vortices, driven by velocity induction. A comparison of our simulation results with towing-tank experiments will be submitted for journal publication [17].

II. Numerical Setup

A. Numerical Method

The LES is performed using the incompressible Navier–Stokes code MGLET developed at Technical University of Munich for solving the Navier–Stokes equations and the continuity equation [18]:

$$\frac{\partial u_i}{\partial t} + \frac{\partial (u_i u_j)}{\partial x_j} = -\frac{1}{\rho_0}\frac{\partial p'}{\partial x_i} + (\nu_{\text{mol}} + \nu_{\text{turb}})\frac{\partial^2 u_i}{\partial x_j^2} \tag{1}$$

$$\frac{\partial u_j}{\partial x_j} = 0 \tag{2}$$

Here, u_i represents the velocity components in three spatial directions ($i = 1, 2,$ or 3), and $p' = p - p_0$ equals the deviation from the reference state p_0. Molecular viscosity ν_{mol} is set to $2.29 \cdot 10^{-2}$ m^2/s, and the eddy viscosity ν_{turb} is obtained by means of a Lagrangian dynamic subgrid-scale model [19]. For density, $\rho_0 = 1.2$ kg/m^3 is employed. Equations (1) and (2) are solved by a finite-volume approach using a fourth-order finite-volume compact scheme [20]. The simulations are performed in parallel using a domain-decomposition approach.

B. Initial Vortex Pair

The fully rolled-up wake vortices are initialized by superposition of a pair of counter-rotating Lamb–Oseen vortices with a circulation of $\Gamma_0 = 530$ m^2/s, a vortex core radius of $r_c = 3.0$ m and a vortex separation $b_0 = 47.1$ m, which are representative values for a generic heavy aircraft [1]. We employ a relatively large core radius of 6.4% of b_0, because in numerical simulations, regions with steep velocity gradients have to be resolved well to limit numerical dispersion [21]. General vortex behavior is little affected by the relatively coarse initial core radius. This is a highly idealized model, because aircraft in landing configuration with flaps and slats deployed generate complex wakes consisting of at least four vortices. Depending on the aircraft type, vortex separation in a high-lift configuration may be smaller than it may be expected for elliptical wing loading [22]. The initial height of the vortex pair is set to $h_0 = b_0$. The Reynolds number is set to $Re_\Gamma = \Gamma_0/\nu = 23,130$. The molecular viscosity of air of $13.5 \cdot 10^{-6}$ m^2/s corresponds to a Reynolds number of $3.9 \cdot 10^7$. The velocity scale is based on the initial descent speed of the vortex pair $V_0 = \Gamma_0/2\pi b_0 = 1.79$ m/s. This defines the nondimensional time $t^* = t\frac{V_0}{b_0}$ with $t_0 = b_0/V_0 = 26.3$ s and nondimensional vorticity $\omega^* = \omega t_0$. For prescribing the initial vortex velocity field, six image vortex pairs in the spanwise direction and two mirror vortices in the direction perpendicular to the ground are taken into account (Fig. 1).

C. Computational Domain

In our simulations, we use two different domain sizes. The dimensions are either $L_x = 192$ m, $L_y = 384$ m, $L_z = 144$ m (Fig. 2) or $L_x = 384$ m, $L_y = 288$ m, $L_z = 96$ m. This corresponds to approximately $4b_0 \times 8b_0 \times 3b_0$ or $8b_0 \times 6b_0 \times 2b_0$, respectively. We impose periodic boundary conditions in the flight direction x and the spanwise direction y. A no-slip condition is set at the ground at $z = 0$ and a free-slip condition at the top at $z = z_{\max}$. The number of grid points are $N_x = 256$, $N_y = 512$, $N_z = 256$ or $N_x = 512$, $N_y = 384$, $N_z = 192$, respectively, leading to a total of 33.5 and 37.7 millions grid points. We employ a horizontally equidistant mesh. In the vertical direction, the mesh is stretched geometrically up to a height of b_0 and then is continued equidistantly until the top of the domain.

We impose obstacles at the ground surface with square-shaped and rectangular cross section of 9×9 m or 9×4.5 m. Obstacles at the ground surface are introduced to trigger the formation of secondary vorticity structures (SVSs) and to achieve early vortex decay. For numerical reasons, we cannot set the velocity inside the obstacle to zero. Instead, the obstacles are modeled by adding a drag force source term $F_{D,i} = C_D|u|u_i$ to the Navier–Stokes equations with a large drag coefficient $C_D = 10$.

Two different domain sizes are used to investigate different effects to save computational costs. The first one focuses on the effect of crosswind and the interaction of the obstacle with the wake vortices. Only for relatively small times the obstacle can be regarded as independent. After the disturbances have reached the boundary, the setting is representing the effect of periodically arranged obstacles. The second domain nearly covers a Crow wavelength of $8.4b_0$ and allows investigating obstacle effects for larger times, until again edge effects appear.

D. Ambient Wind

To provide a realistic environment, we establish a turbulent wind in a separate simulation. This way, we introduce time-dependent

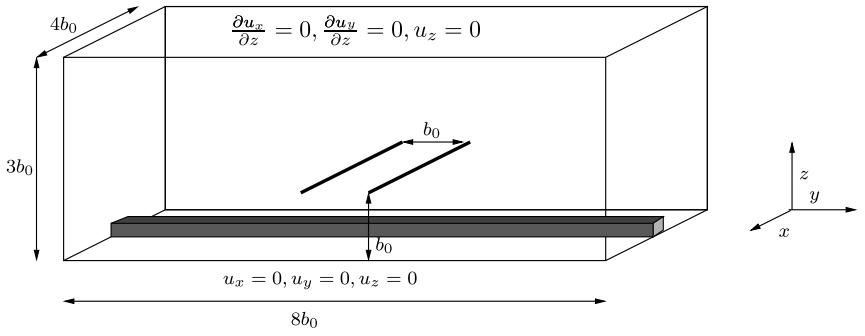

Fig. 2 Schematic of the computational domain showing the initial vortex position and an obstacle.

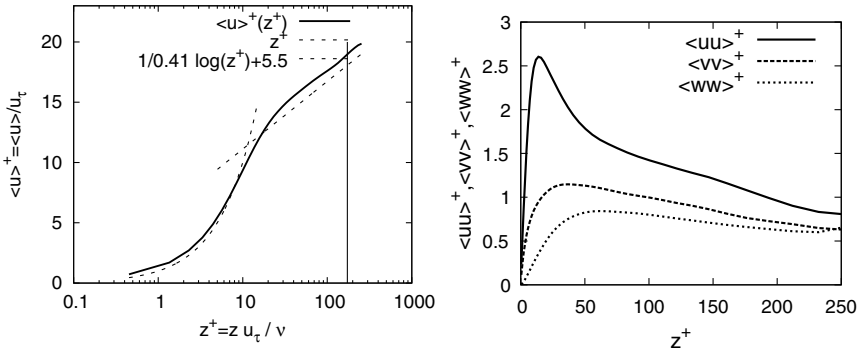

Fig. 3 Mean velocity profile and velocity fluctuations characterizing the separately simulated turbulent wind and the initial vortex position.

velocity fluctuations modeling the atmospheric boundary layer physically. We simulate a turbulent half-channel flow with $Re_\tau = 530$ applying a free-slip condition at the top of the domain [23]. Prescribing initially a vertical wind profile following the universal logarithmic law and imposing a streamwise pressure gradient of $\mathrm{d}p/\mathrm{d}y = 5.9 \cdot 10^{-5}$ N/m^3, the wind flow is driven through the computational domain. We let the flow develop until characteristic wall streaks appear and an equilibrium between the pressure gradient and the wall friction is established. Averaged wind profile $\langle u^+ \rangle$ and velocity fluctuations $\langle uu \rangle^+$, $\langle vv \rangle^+$, $\langle ww \rangle^+$ (see Fig. 3) converge to the typical half-channel flow characteristics [23]. The time-averaged streamwise velocity of the wind at the initial vortex height is $0.85V_0 = 1.52$ m/s, where V_0 is the initial vortex descent speed.

A recapitulation of the basic properties of the channel flow (shown in [24]) is as follows. Let δ denote the channel half-height and consider the following quantities as averaged in time. For the boundary-layer approximation, the Navier–Stokes equations yield the wall shear stress $\tau_w = -\delta \cdot \partial p/\partial x$, with constant pressure in wall-normal direction. The wall friction velocity is defined by $u_\tau = (\tau_w/\rho)^{1/2}$. This yields the normalized values $u^+ = u/u_\tau$, $z^+ = zu_\tau/\nu$ and an intrinsic Reynolds number $Re_\tau = u_\tau \delta/\nu$. The boundary layer of a turbulent flow has now three characteristic parts: the viscous sublayer, the transition layer, and the logarithmic layer (see Fig. 3). In normalized coordinates, the mean wall profile is independent of the Reynolds number. Thus, in the case of realistic Reynolds numbers, we have a very thin viscous sublayer and no significant changes of the mean flow in the region of vortex initialization. In a fully developed flow, each region has its own flowfield characteristics. The viscous sublayer is shaped by coherent structures, so-called near-wall streaks. For Reynolds numbers $Re_\tau < 1000$, these near-wall streaks are proven to have a spanwise spacing of $\lambda^+ \sim 100$ [25]. To resolve the viscous sublayer, wall-resolved LES requires a stretched mesh in the wall-normal direction, with $z^+_{\min} < 1$. This limits our simulations to $Re_\tau = 530$ and $Re_\Gamma = 23,130$. To consider higher Reynolds numbers, a wall model is needed. We employ the Grötzbach wall model (case 2 in Table 1) that locally computes the wall shear stress τ_w based on the logarithmic law to establish realistic velocity profiles [26].

Table 1 Performed simulations and parameters of the numerical setup

Case	Domain	Obstacle	Wind	h_0	Re_Γ
1	$4b_0 \times 8b_0 \times 3b_0$	No obstacle	c/w	b_0	$2.313 \cdot 10^4$
2	$4b_0 \times 8b_0 \times 3b_0$	No obstacle	c/w	b_0	$2.313 \cdot 10^5$
3	$4b_0 \times 8b_0 \times 3b_0$	$0.2b_0 \times 0.2b_0$ block	c/w	b_0	$2.313 \cdot 10^4$
4	$8b_0 \times 6b_0 \times 2b_0$	$0.2b_0 \times 0.2b_0$ block	No wind	$b_0/2$	$2.313 \cdot 10^4$
5	$8b_0 \times 6b_0 \times 2b_0$	$0.2b_0 \times 0.1b_0$ block	No wind	b_0	$2.313 \cdot 10^4$
6	$8b_0 \times 6b_0 \times 2b_0$	$0.2b_0 \times 0.1b_0$ plates	No wind	b_0	$2.313 \cdot 10^4$
7	$8b_0 \times 6b_0 \times 2b_0$	$0.2b_0 \times 0.1b_0$ plates	h/w	b_0	$2.313 \cdot 10^4$

E. Listing of Simulations

A listing of the conducted simulations is given in Table 1. In Sec. III, we present simulation results starting with an analysis of wake-vortex decay mechanisms in the situation of a flat ground (case 1). The effect of the Grötzbach wall model and an increased Reynolds number is investigated in Sec. IV (case 2). In Sec. V, we study the effect of an obstacle and how it enhances wake-vortex decay by comparing cases 1 and 3. We quantify the accelerated decay and describe the underlying vortex dynamics. Further, we study the simplified setup of case 4 without environmental turbulence to point out the flowfield characteristics. Finally, in Sec. VI, we examine different obstacle geometries to optimize them with respect to size and shape (cases 5, 6, and 7) and the influence of headwind (case 7).

III. Wake-Vortex Evolution with Flat Ground

A. Flow Phenomenology

In the early phase, the approach of a vortex pair to a planar wall can be regarded as two-dimensional. Early achievements in the framework of inviscid theory, which treat the boundary as free slipping, imply a monotonic descent of the vortices on hyperbolic trajectories [27,28]. However, a viscous boundary layer changes the flow characteristics strongly [24].

When the vortex pair descends, it induces a vorticity layer at the ground (Fig. 4) [8]. An adverse pressure gradient builds up in the boundary layer while the primary vortices are diverging. The boundary layer bifurcates with a layer remaining close to the wall and a layer growing from the surface, which finally rolls up into secondary vortices and separates [29]. From numerical simulations as well as field measurement campaigns [4], we observe a minimum descent height of about $b_0/2$ (assuming the vortices are initialized sufficiently aloft) at the instant when secondary vortices detach from the ground.

Crosswind also induces vorticity at the ground, which has the opposite sign of the vorticity layer induced by the upwind vortex and the same sign as the vorticity layer induced by the downwind vortex (Fig. 5). Thus, the crosswind vorticity supports the formation of the downwind vorticity layer and attenuates the upwind vorticity layer. As a consequence, vorticity layers generated by the wake vortices become unequally strong, and the upwind and downwind vortices behave asymmetrically. The magnitudes of the wake-vortex induced vorticity layers are growing, leading eventually to separation and the generation of counter-rotating secondary vortices, first at the downwind and then at the upwind vortex. Then, the secondary vortices rebound and interact with the primary vortices, which we will discuss in detail. We also observe that the turbulent structures (streaks) of the wind boundary layer are entrained during the roll-up while these structures are cleared out at the ground between the vortices (Fig. 4a).

B. Trajectories and Decay

Knowledge and prediction of the position and the strength of the wake vortices is important for a WVAS [30]. In the LESs, primary and secondary vortex centers can be tracked. This is done by detecting local pressure minima and extreme values of vorticity. Results for the

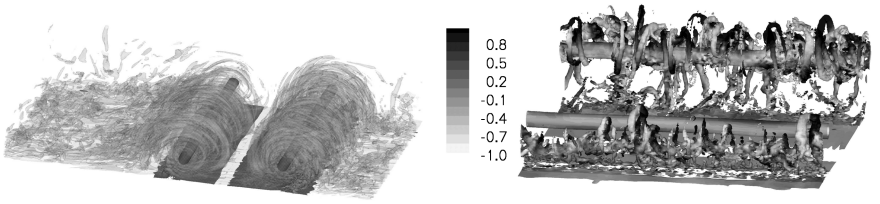

a) $t^* = 1.3$ b) $t^* = 1.8$

Fig. 4 Wake-vortex pair in crosswind situation: a) vorticity isosurfaces $\|w^*\| = 31.4$ (black) and 3.14 (gray), b) vorticity isosurfaces of $\|w^*\| = 39.4$ colored by vorticity strength in spanwise direction showing hairpin vortices (case 1).

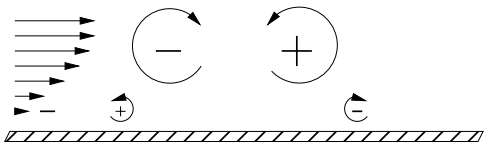

Fig. 5 Sketch of wake-vortex flow with crosswind.

axially averaged vortex core trajectories are displayed in Fig. 6 and compared with predictions of the Deterministic and the Probabilistic Two-Phase wake-vortex decay and transport model (D2P, P2P) [4,31].

In the LES results, it is seen that the wake vortices descend somewhat deeper, and the final vertical and lateral offsets are smaller than in the deterministic real-time predictions. Clearly, Fig. 6 shows that the LES curves reside well within the probabilistic model predictions at 2σ (95.4%) envelopes. The averaged normalized closest approach to the ground of the LES primary vortices is 0.49 for the upwind and 0.57 for the downwind vortex. Lidar measurements at Frankfurt Airport indicate average minimum altitudes of 0.525 and 0.62, respectively, in corresponding crosswind situations [4]. The measured lateral displacement of the primary vortex trajectories scatters around a median of 3.2 at average vortex ages of $t^* = 3$ [32]. The LES results show a lateral displacement of 3.2 at a time of $t^* = 3$. This good agreement may indicate that the LES results are representative for wake-vortex evolution in ground proximity.

Of particular interest is the vortex strength that ultimately might affect a following aircraft. As a common measure of the vortex intensity for aircraft with sufficiently large wingspans, we consider $\Gamma_{5-15} = 0.1 \int_{5\,\mathrm{m}}^{15\,\mathrm{m}} \Gamma(r)\,\mathrm{d}r$ for the primary and $\Gamma_{r=5\,\mathrm{m}}$ for the secondary vortices, where $\Gamma(r) = \oint \mathbf{u} \cdot \mathrm{d}\mathbf{s}$ denotes the circulation around a circle of radius r centered in the vortex core [33]. The evolution of these quantities is shown in Fig. 7. For early times, where the wake vortices are located at the most critical point hovering over the runway, the circulation remains almost constant. Then, the phase of rapid decay sets in for the upwind vortex at $t^* = 1.5$ and for the downwind vortex at 1.9 shortly after the secondary vortices have reached a maximum strength. Finally, the circulation decay rate is reduced, which is again more pronounced for the downwind vortex. Remarkably, in spite of the rapid decay between $t^* = 1.5$ and 3, the core radius of the primary vortices, defined as the averaged distance from vortex center to the point of maximal tangential velocity, is shrinking temporarily, as shown in Fig. 7 (right), before it starts to grow steadily. The high viscosity and numerical dispersion cause unrealistically high growth rates of the core radius [21]. Until a time of $2t_0$, we see the characteristic core growth rate ($\sim C\sqrt{t}$) for the used LES code. Between $2t_0$ and $3t_0$, we observe a temporal shrinking of the core radius due to the interaction with the secondary vortices. After $3t_0$, the growth roughly continues at the characteristic rate.

C. Wake-Vortex Decay Mechanism

In contrast to the wake-vortex decay mechanisms that appear aloft, which are driven by atmospheric turbulence and thermal stratification [34,35], an important origin of turbulence here is the no-slip condition at the ground (i.e., the strong shear established between the

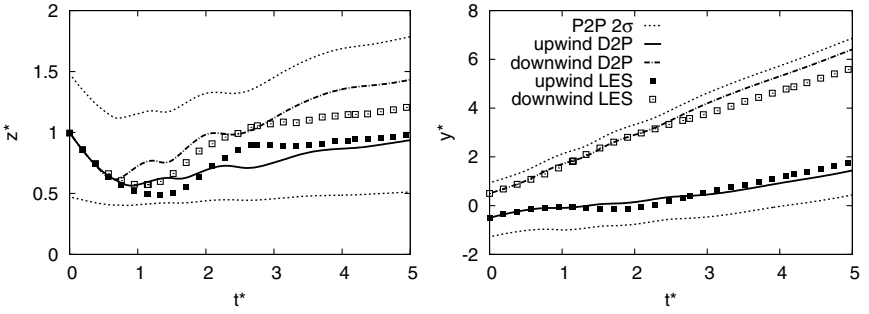

Fig. 6 Normalized vertical and lateral vortex positions of wake vortices in crosswind situation. Results from LES (case 1) compared with deterministic predictions from D2P and 2σ envelopes from P2P wake-vortex model.

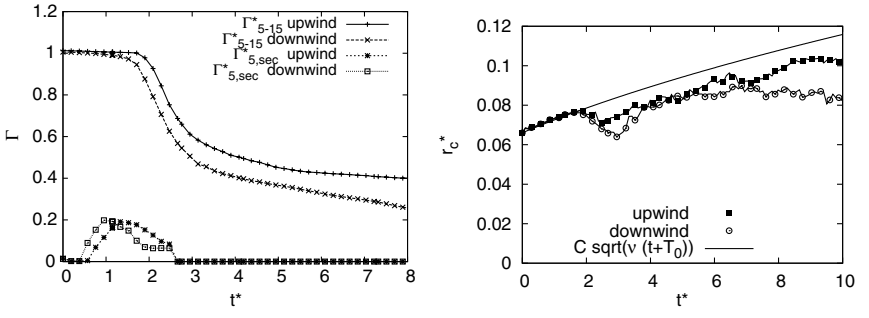

Fig. 7 Evolution of vortex circulation for primary and secondary vortices (left) and core radius with characteristic core growth for LES code (right) (case 1).

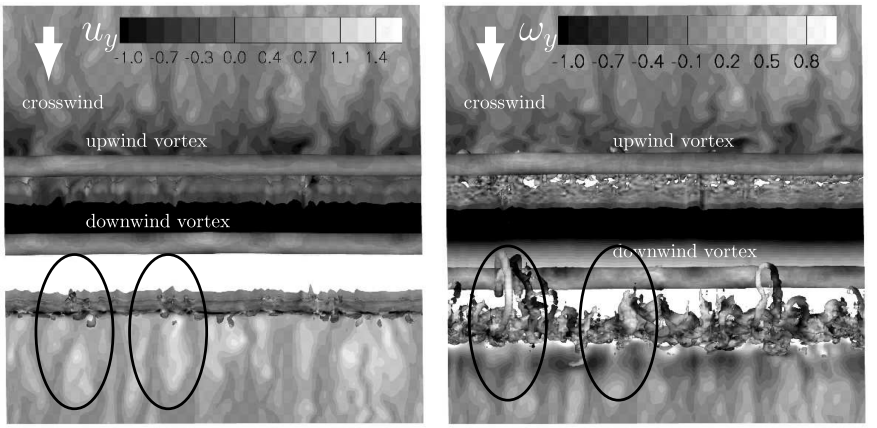

a) t^* = 0.95 **b) t^* = 1.52**

Fig. 8 Velocity irregularities at the ground (streaks) trigger hairpin vortices at secondary downwind vortex. Isosurface of vorticity magnitude $\|w^*\| = 39.4$ combined with velocity at the ground showing regions of strong crosswind (case 1).

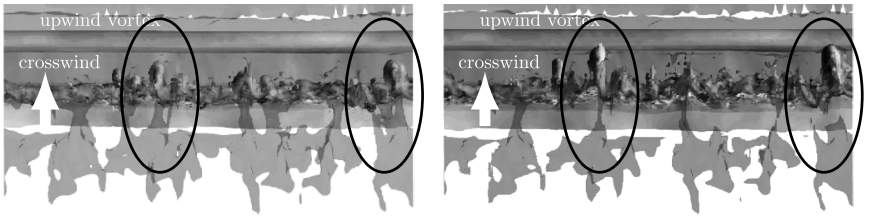

a) t^* = 1.61 **b) t^* = 1.71**

Fig. 9 Velocity irregularities at the ground trigger hairpin vortices at secondary upwind vortex. Isosurface of vorticity magnitude $\|w^*\| = 39.4$ with isosurface of velocity $u_y^* = 0.06$ (translucent) showing regions of weak crosswind (case 1).

free crosswind flow and the zero velocity directly at the ground surface). The generated counter-rotating secondary vortices eventually develop into relatively strong turbulent structures initiating rapid vortex decay. Figure 4b shows that the secondary vortices do not detach homogeneously from the ground but that hairpin vortices or omega-shaped vortices detach at distinct positions and then wrap around the primary vortices. As explained previously, this occurs first at the downwind and then at the upwind vortex. To our knowledge, this phenomenon has not been well documented and explained. Thus, we examine the origin of these instabilities in our simulations.

A closer look at the velocity distribution at the ground, before imposing the vortex system, reveals a wave-shaped pattern of highly elongated structures, the so-called streaks seen in Fig. 8 [25]. These streaks correspond to regions of high velocities oriented in the crosswind/spanwise direction (u_y) in immediate ground proximity. Regions of high crosswind velocity (gradients) and low crosswind velocity (gradients) at the ground strengthen or weaken the roll-up process of the secondary vortices, respectively (Fig. 5).

Thus, a region of small vertical wind gradients at the upwind secondary vortex (Fig. 9) and a region of high wind gradients at the downwind secondary vortex (Fig. 8) both influence the secondary vortices to detach earlier. The shape and development of the omega loops are clearly visible in Fig. 8 at the downwind vortex, whereas the correlation of the boundary-layer streaks and the omega loops is even more obvious for the upwind vortex, as shown in Fig. 9.

As a consequence, a correlation of the crosswind instabilities in the boundary-layer flow and the secondary vortex disturbances should be expected. In the LES computations, the crosswind instabilities correspond to streaks with a spacing $\lambda^+ \sim 100$ ($\lambda \sim 27$ m), which is found in experiments [36] as well as in numerical simulations for a relatively large molecular viscosity [25]. Butler and Farrell [37] give evidence that $\lambda^+ \sim 100$ also holds for a small molecular viscosity. Consequently, the disturbances of the secondary vortices are highly dependent on the molecular viscosity. Hence, for a molecular viscosity of air, the streak spacing would be on the order of centimeters, which is insignificant for wake vortices. We suppose that, in reality, inhomogeneities of the ground on the order of several meters may cause similar crosswind gradients at the ground surface, leading to similar decay scenarios as observed at $Re_\tau = 23,130$. Unfortunately, limitations of computational resources limit wall resolving LES to relatively low Reynolds numbers, whereas wall models do not yield the required coherent structures. The following list provides a description of wake-vortex decay in ground proximity broken down to five steps, where the different items will be discussed in detail in Sec. V.C:

1) The formation of secondary vortices is favored at crosswind velocity excesses or deficits for the downwind and upwind vortex,

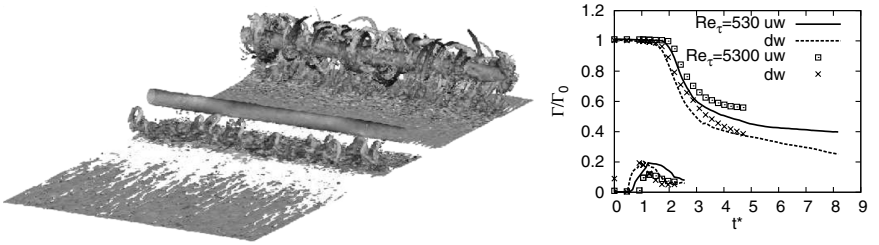

Fig. 10 Isosurface of vorticity magnitude $\|w^*\| = 39.4$, colored by vorticity in spanwise direction, at $t^* = 1.66$, case 2 (left), vortex circulation for primary and secondary vortices for different values of Re, case 1 and 2 (right).

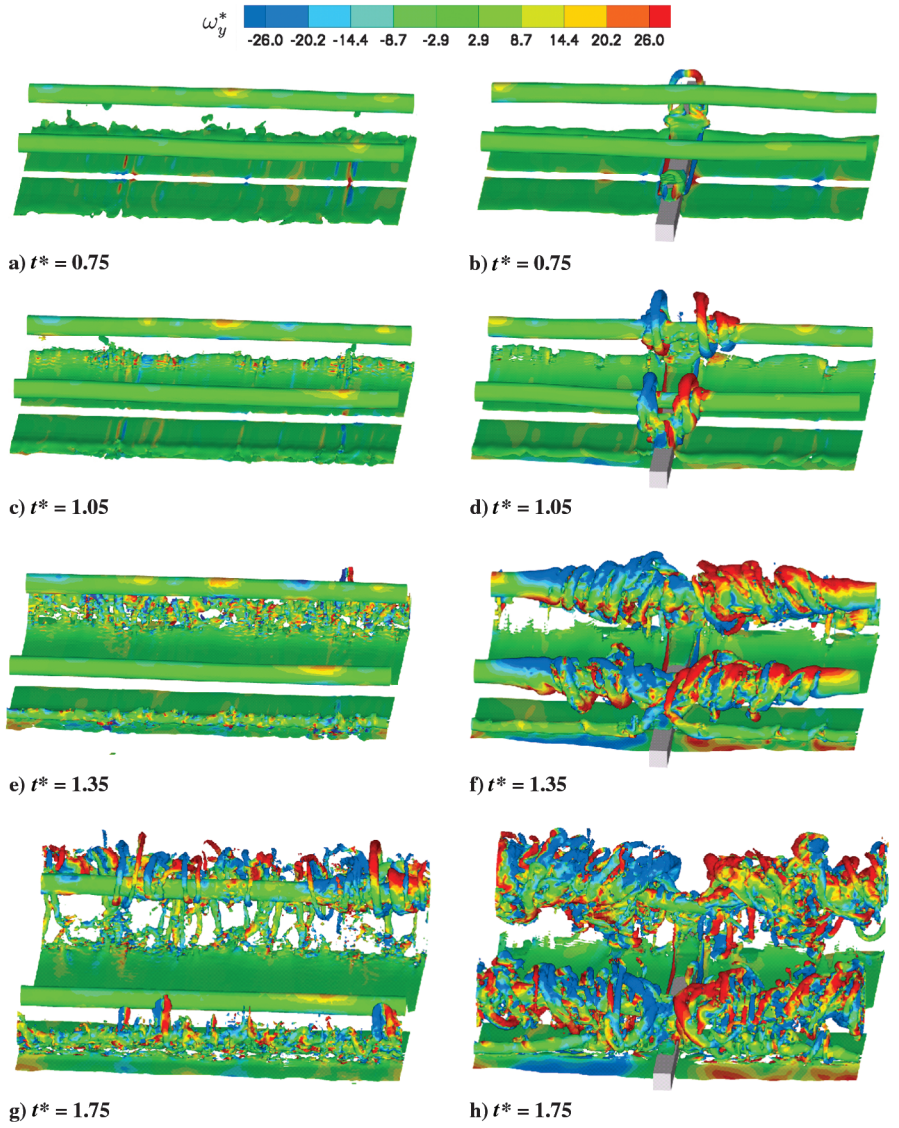

Fig. 11 Wake-vortex evolution with crosswind without, case 1 (left), and with square-shaped obstacle, case 3 (right), at the ground. Isosurfaces of $\|w^*\| = 39.4$ colored by vorticity strength ω_y^* in the spanwise direction.

respectively, and can be triggered by perturbations like crosswind streaks.

2) The subsequent stretching and tilting of the secondary vortices by the primary vortex causes intense omega loops (hairpin vortices).

3) Omega-shaped secondary vortex approaches the primary vortex by self-induction.

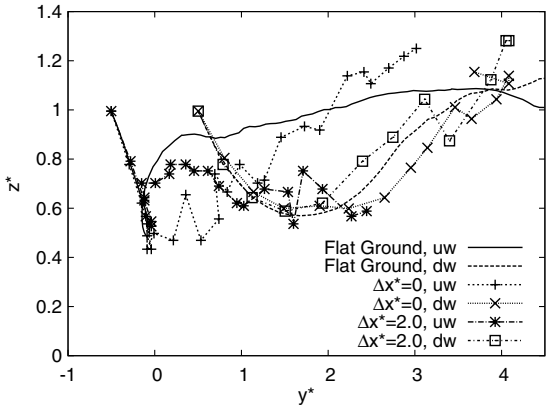

Fig. 12 Vortex center trajectories for flat ground and different distances from an obstacle with $0.2b_0 \times 0.2b_0$ cross section. Symbols starting at $t^* = 0$ and proceeding with steps of $0.3t_0$ (cases 1 and 3).

4) After the secondary vortex has looped around the primary vortex, the omega head widens, driven by self-induction.

5) The interaction of approaching secondary vortices and primary vortex causes turbulence and annihilation of vorticity.

The prominent role of secondary vorticity structures for wake-vortex decay is well known and has also been analyzed in detail in [35]. The formation of omega loops from secondary vortices has been studied in [38]. We will have a closer look at these mechanisms when we investigate the effect of obstacles at the ground. An idealized development of a strong omega loop can be seen in Sec. V.C.

IV. Effect of a Wall Model in High-Reynolds-Number Flows

In this section, we discuss the problems of Reynolds number effects and the use of a wall model. A simulation with $Re_\Gamma = 231,300$ and $\nu = 2.29 \cdot 10^{-3}$ m^2/s is used to investigate the Reynolds number dependence of vortex decay. For this purpose, we impose the Grötzbach wall model [26] based on the logarithmic wall law to achieve the characteristic boundary-layer velocity profile in the presimulation. Again we use a pressure-driven flow with the same pressure gradient $\mathrm{d}p/\mathrm{d}y = 5.9 \cdot 10^{-5}$ N/m^3 as before. As expected, the spacing between the detaching SVS becomes much smaller (Fig. 10, left), and the SVSs are not well resolved. The vortex decay at a Re, which is 10 times larger, appears to follow the same physics but is somewhat delayed, and the circulation after decay remains slightly

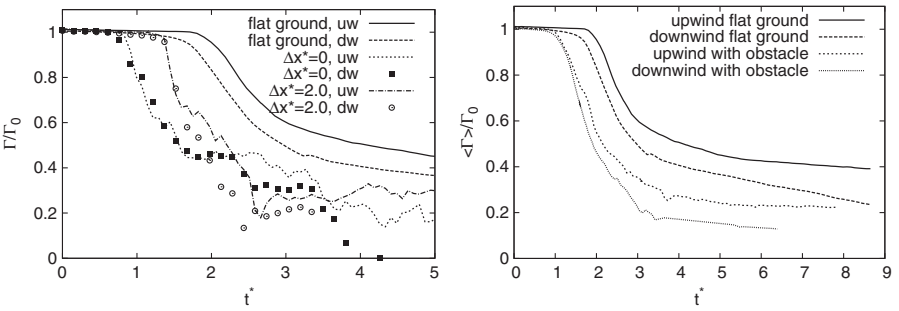

a) b)

Fig. 13 Vortex circulation Γ_{5-15} in crosswind situation with flat ground or obstacle with $0.2b_0 \times 0.2b_0$ cross section at a) different positions, and b) axially averaged (cases 1 and 3).

higher than in the low-Reynolds-number case (Fig. 10, right). The attenuated decay supports the idea stated in the previous sections that coherent structures generated at the ground (i.e., excesses and deficits in the boundary-layer velocity) promote wake-vortex decay.

From the last two sections, we see that the vortex decay of wake vortices in ground proximity strongly depends on the instabilities of the secondary vortices. Thus, the decay depends on the irregularities of the turbulent crosswind at the ground. In [39], the requirements for resolving crosswind streaks in a situation of flat ground are discussed. Obviously, for realistic Reynolds numbers, the current computing power does not enable us to resolve the viscous sublayer. Without massive grid refinement, the interesting structures would all dissolve inside the first grid cell. To the authors' knowledge, it is an open question how to model the effect of the unresolved streaks on the vortex flow. In reality, the ground surface close to the runway never is ideally flat. Always-existing surface irregularities will instead affect the boundary-layer flow such that the crosswind excesses and deficits that trigger instabilities of the secondary vortices will emerge at different scales, depending on the local surface and meteorological conditions. Therefore, for future work, we propose to model reasonable instabilities explicitly.

V. Obstacle Effect

A. Flowfield

In this section, we compare wake-vortex flows above flat ground with flow above ground with obstacles both under the influence of a crosswind. When we impose an obstacle at the ground surface, the flow changes substantially. At the top of the barrier, secondary vorticity is generated rapidly after vortex initialization, which subsequently detaches and develops into a distinct loop, as shown in Fig. 11 (right). The loop is stretched and winds around the primary vortex form an omega-shaped loop, approaching and immersing itself into the primary vortex. The process follows the vortex stretching and tilting mechanisms detailed in [35]. The geometrically induced SVSs travel along the primary vortices driven by self-induced velocity induction while they weaken the primary vortices efficiently, as we show next in detail. In Fig. 11 (left), we see that, for flat terrain, the separation process just begins at a time of $t^* = 1.35$. By this time, with an obstacle at the ground, substantial disturbances engulf the primary vortices (Fig. 11, right).

B. Trajectories and Decay

Now, we analyze the enhanced decay characteristics quantitatively. Furthermore we are interested in the change of trajectories (i.e., whether rebound height is influenced by an obstacle or not). We have to keep in mind that we use periodic boundary conditions. Thus, interpreting the simulations correctly, we do not consider the influence of one single obstacle but periodically arranged obstacles with a separation equal to the domain length of $4b_0$. However, until the disturbance reaches the domain boundary, we can neglect the influence of the adjacent obstacles. Because of the intense interaction of primary and secondary vortices, it becomes very difficult to track the vortices in the flow with obstacles, especially the downwind vortex, for larger times than $t^* = 3$.

Lateral advection of the primary vortices plays an important role for the clearance of the flight corridor during final approach. Because of the weak crosswind, the upwind vortex may hover above the runway for a long time, as depicted in Fig. 12. This is a potentially hazardous situation for following aircraft. We see that an obstacle does not change that fact. Above flat ground, the primary vortices can rebound to a height of about $1.1b_0$. Directly above the obstacle, the rebound height is much reduced but can exceed the height above flat ground at later times when circulation is already much reduced (Fig. 13). In a distance of $x^* = 2.0$, the rebound remains consistently below that with flat ground.

Above the obstacle, we observe a tremendous and rapid reduction of the circulation to 40% of the initial circulation (Fig. 13a), whereas, in the case of a flat ground, the circulation does not change significantly in this early time period. We further observe that, within a distance of $2b_0$ from the obstacle, the circulation is also reduced faster. Because the decay does not develop uniformly along the vortex filament, we compare wake-vortex decay with flat ground by averaging Γ_{5-15} in axial directions. During the initial descent, the vortex strength remains nearly constant for one t_0, as shown in Fig. 13b. The decay of $\langle\Gamma_{5-15}\rangle$ sets in when secondary vorticity merges with the primary vortices. With crosswind, vortex decay proceeds asymmetrically. The downwind vortex decays faster and reaches lower values than the upwind vortex. With obstacle, the decay process is initiated nearly one t_0 earlier. If we assume that the International Civil Aviation Organization separation of 5 n mile at a medium aircraft following a heavy correspond to 120 s or 4.6 t_0, we read 50% of the initial circulation for the operationally relevant upwind vortex. Figure 13b indicates that the obstacle reduces $\langle\Gamma_{5-15}\rangle$ of the upwind vortex by 50% at a vortex age of $2t_0$, compared to the case without obstacle, where this decay level is only reached two t_0 later.

C. Detailed Analysis of Vortex Dynamics with Obstacle

For clarity, we analyze vortex dynamics triggered by the obstacle without the influence of the crosswind. In [17], we compare the results from LES with towing-tank experiments. There, the initial vortex height is approximately $b_0/2$. Therefore, in this section, the wake-vortex pair is initialized at $b_0/2$.

The following five characteristics of the phenomenon explain how the secondary vortices are generated at the ground, how they approach the primary vortices, and how their interaction with the primary vortices can be substantially accelerated to achieve early vortex decay.

1) Strong omega-shaped secondary vortices detach early. Depending on the obstacle height, secondary vorticity detaches earlier. Because the distance to the primary vortices is smaller than $b_0/2$, the strength of these SVS is also slightly increased (Fig. 11). In our simulations, we find above the obstacle a secondary vortex strength of up to 28% of the primary vortices as opposed to 26% above flat ground.

2) Omega-shaped secondary vortex approaches the primary vortex by self-induction. Once the secondary vortices are perturbed due to

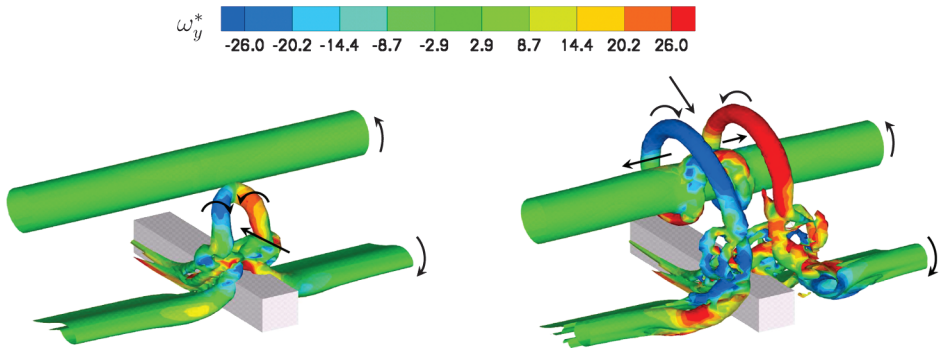

Fig. 14 LES (case 4) shows omega-shaped SVS inducing a velocity toward the primary vortex (left), and inducing streamwise propagation velocity (right). Isosurfaces of $\|w^*\| = 39.4$ colored by vorticity strength ω_y^* in the spanwise direction.

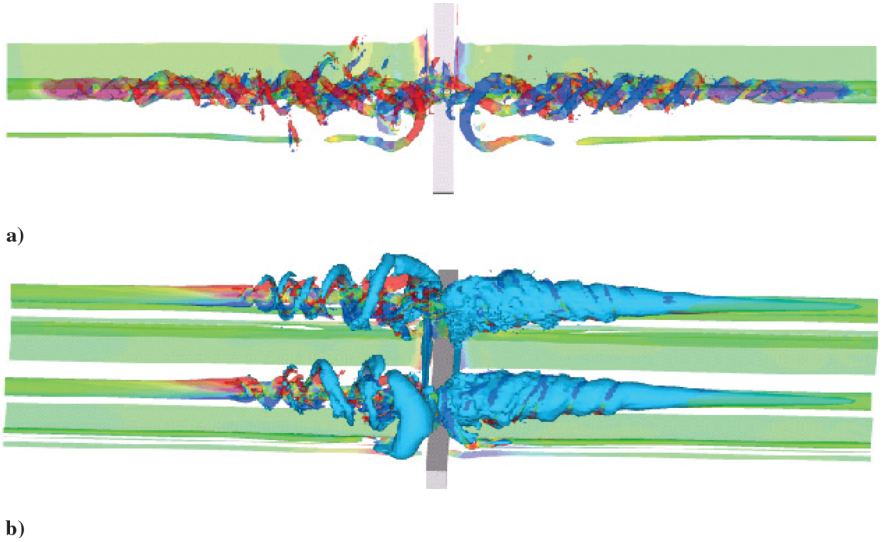

Fig. 15 Isosurface of vorticity magnitude $\|w^*\| = 105.2$ colored with vorticity strength ω_y in spanwise direction: a) forming a double helix at $t^* = 0.84$, and b) with isosurface of axial velocity $u_x^* = 0.56$ at $t^* = 0.61$ (case 4).

the obstacle (or other instabilities), the flow can no longer be considered as two-dimensional. The early detachment of the vorticity layer above the obstacle leads to an omega-shaped SVS, as shown in Fig. 14. Figure 14 (left) reveals the physical mechanism of how the hairpin vortex induces a velocity to itself moving toward the primary vortex. This speeds up the interaction between the vortices. Simultaneously, the omega-shaped SVS is stretched and bent around the primary vortex by its velocity field, as detailed in [35]. Subsequently, the spirally moving secondary vortex induces itself a propagation velocity along the primary vortex similar to free vortex rings (Fig. 14 right).

3) After the secondary vortex has looped around the primary vortex it travels along the primary vortex again driven by self-induction. The helically looped SVS propagates up and down along the primary vortex, where the two vortices are merging to a single highly turbulent vortex (Fig. 11). The secondary vortex also deforms the primary vortex. In that process, the secondary and primary vortices take the shape of a screw, and a double helix is created, larger and wider at the basis above the obstacle (Fig. 15a).

In this phase, we identify two complementary effects, leading to an axial velocity inside the vortex, as shown in Fig. 15b. Similar effects are also known as end effects that were observed in test facilities with finite length [16].

a) When the primary and secondary vortices are transformed into a double helix, both vortices have the same sense of rotation and helicity and consequently induce an axial velocity to the same side inside the double helix (blue cone in Fig. 15b).

b) We also observe an axial velocity in the vortex core in regions far ahead of the helix (Fig. 15b). The second effect is initiated by a reduction of the circulation above the obstacle (Fig. 16) that locally increases the pressure in the vortex core. This corresponds to a pressure gradient within the vortex core in axial directions, inducing axial velocities (Fig. 16) where the locally averaged pressure and velocity in flight direction at the vortex center are depicted. The pressure disturbance starts at a time of $t^* = 0.08$ and reaches the domain boundary at a time of $t^* = 0.53$, corresponding to a propagation speed of $U_p^* = 8.8$. The propagation of pressure disturbances in Lamb–Oseen vortices has been thoroughly investigated in [40].

Stephan et al. [41] indicate that similar phenomena as described here also occur when the aircraft touches down on the tarmac. The end effects can occasionally be observed when condensation trails marking the vortex cores adopt helical shapes and quickly disappear after touchdown.[§,¶] Condensation trails may occur when the temperature, lowered by the pressure decrease in the vortex core, leads to supersaturation of water vapor and thus to condensation. Thus, the rapid disappearance of the condensation trail is directly related to the pressure and consequential temperature increase in the vortex cores.

The knowledge of the propagation speed of the disturbance and the related rapid decrease of circulation is crucial for practical applications at airports where the decay of wake vortices close to the touchdown zone and suitable distances between adjacent obstacles need to be determined. The spiral disturbance can be approximated as a ring at least during the first stage of its roll-up. Vortex rings move with a self-induced velocity in the direction of the flow inside the ring. The propagation speed depends on the ring radius R, the core

[§]Data available online at http://www.youtube.com/watch?v=oHGqxM1-rAI [retrieved 15 April 2013].

[¶]Data available online at http://www.youtube.com/watch?v=KqU70RORXtA [retrieved 15 April 2013].

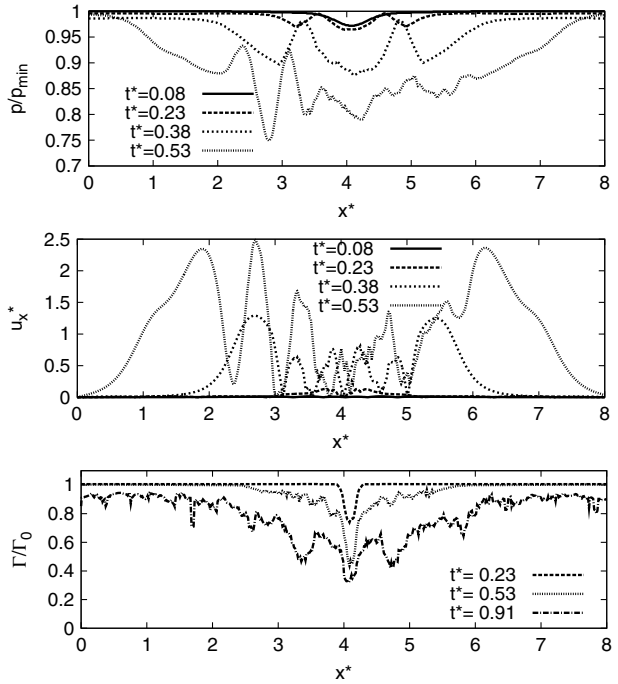

Fig. 16 Distribution of $\langle p\rangle/p_{\min}$,$\langle u_x\rangle^*$, and $\Gamma^*_{5\text{–}15}$ along the vortex center at different times (case 4).

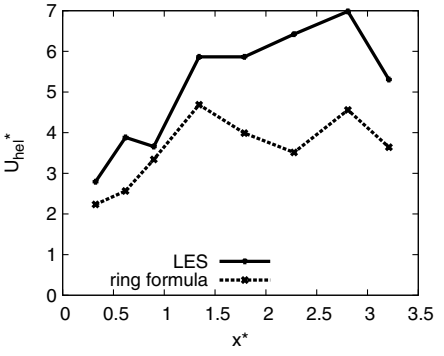

Fig. 17 Propagation speed of helix compared with theoretical speed of a vortex ring.

radius a, and the circulation Γ of the ring vortex. Neglecting viscosity, the induced propagation speed of a thin vortex ring can be computed with the following formula [27]:

$$U = \frac{\Gamma}{4\pi R}\left(\log\frac{8R}{a} - 0.25\right) \tag{3}$$

To determine the propagation speed, we consider the helix head (see for example Fig. 15b) and estimate a core radius of $0.02b_0$. We further evaluate the circulation and ring radius of the secondary vortex at different locations to compute the propagation speed according to Eq. (3), shown in Fig. 17. Apparently, Eq. (3) underestimates the propagation speed. In particular, in the later stage, the double helix propagates at a higher speed compared to a simple vortex ring. Potentially, the conical shape of the double helix as well as the helical shape of the primary vortex causes higher induced velocities. For the design of obstacle separations at an airport, Eq. (3) may provide a conservative approximation of the propagation speed of the disturbances. Scaling of Eq. (3) allows estimating the propagation velocity for different aircraft types. The interaction of disturbances caused by more than one obstacle is investigated in [17].

4) Dedicated secondary vortex remains connected to the regular ground effect vortex and thus obtains continued supply of energy. As we can see in Fig. 14, the secondary vortex detaches much faster above the obstacle. However, it stays connected in accordance with the third Helmholtz law stating that a vortex tube cannot end within a fluid. It must either end at a solid boundary or form a closed loop. Isosurfaces of vorticity magnitude in Fig. 15 show the connected secondary vortex.

5) Highly intense interaction of primary and secondary vortices leads to rapid wake-vortex decay. The decay rates of wake vortices highly depend on the interaction with their environment [35]. The circulation decreases while the primary vortex is conducting work on SVS and merging. The stronger the SVS, the faster the vortex decay. In ground proximity, distinct SVSs evolve that trigger vortex decay close to ground. Obstacles lead to an earlier interaction of even higher intensity than the flat ground, which was quantified in Sec. V.B.

The previously identified five flow features describe how obstacles at the ground may induce rapid wake-vortex decay independently of natural external disturbances.

VI. Effects of Different Obstacle Geometries and Headwind

In this section, we discuss the shape and the size of the obstacles. In our baseline setting, we use $0.2b_0 \times 0.2b_0$ square profiles in normalized coordinates, which corresponds to a barrier of 9×9 m square cross section in reality. This appears quite high for realistic applications at airports. Moreover, a massive barrier requires a lot of material and might conflict with safety requirements (e.g., escape routes of departing aircraft). We reduce the obstacle height to $h^* = 0.1$, keeping the width fixed. Furthermore, we reduce the obstacle volume. The idea is to mimic the block shape by thin plates at intervals of $\Delta y^* = 0.45$ (21 m) to achieve a similar effect (Fig. 18).

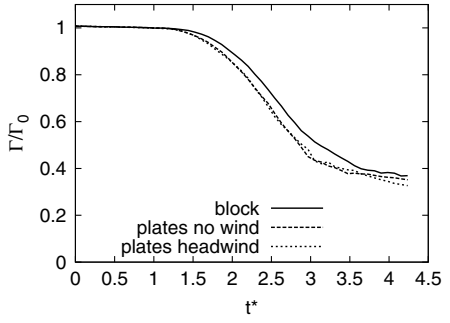

Fig. 19 Evolution of $\Gamma_{5\text{–}15}$ averaged in flight direction for different geometries and wind configurations (cases 5, 6, and 7).

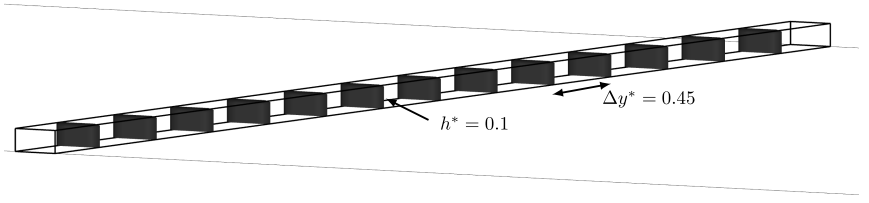

Fig. 18 Schematic representing an obstacle with a $0.2b_0 \times 0.1b_0$ cross section and a corresponding plate line mimicking the obstacle.

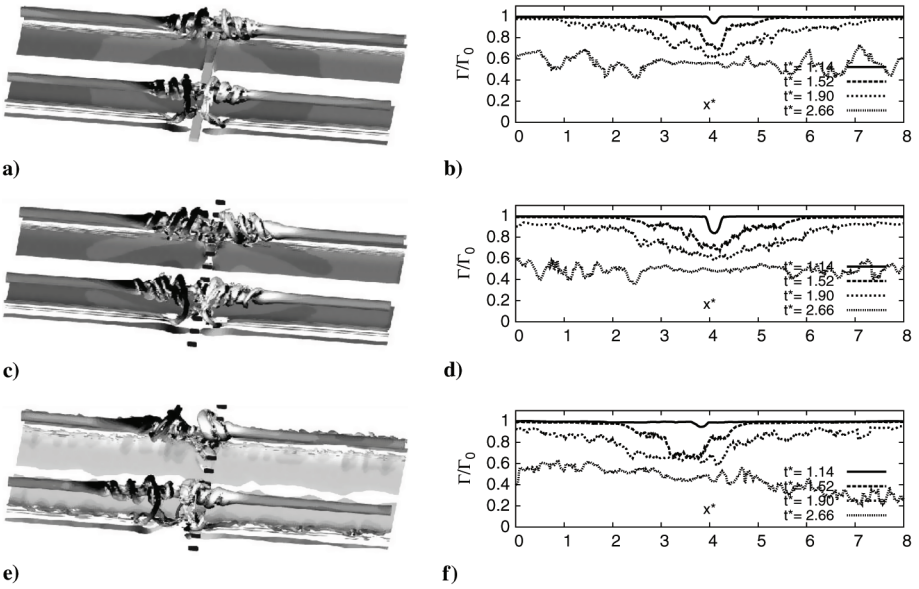

Fig. 20 Isosurfaces of $\|w^*\| = 52.6$ colored by vorticity in spanwise direction at a time of $t^* = 1.52$ (left), axial distribution of Γ_{5-15} at different times (right): a, b) block-shaped obstacle; c, d) plate line; and e, f) plate line with headwind from right to left (cases 5, 6, and 7).

Figure 19 shows that we can reduce the volume of the obstacle without reducing the effects on wake-vortex decay. We see that the decay with the plate line starts even slightly earlier. In Fig. 20 (left), we observe that a plate line leads to similar effects on the secondary vortices as a block-shaped obstacle. SVSs separate even slightly earlier, although their contours are less smooth. The longitudinal circulation distributions look very similar in both cases (Figs. 20b and 20d). We clearly see that, with a plate line, the decay is even faster (Fig. 19).

A plate line raises the question of robustness with respect to headwind advecting the primary and secondary vortices across the obstacles. The headwind shifts the rolled-up SVS; however, each of the listed effects described in Sec. V.C can still be observed (Fig. 20e). Although the headwind shifts the roll-up of the SVS, the effect of the plates appears to be very robust, and the averaged circulation decay is not affected (Fig. 19). The longitudinal circulation distributions (Fig. 20f) are shifted in the direction of the headwind.

VII. Conclusions

Wall-resolved large-eddy-simulation computations to study wake-vortex behavior in ground effect with and without crosswind were conducted. The investigation of the decay mechanisms at $Re_\Gamma = 23.130$ reveals that perturbations of the secondary vortices trigger rapid vortex decay of the primary vortices. It is shown that simple wall modeling does not bring forth the coherent structures in the boundary-layer flow that are critical for rapid vortex decay in ground effect. In addition, it is expected that, at realistic Reynolds numbers, surface irregularities and meteorological conditions will affect the boundary-layer flow and perturb the secondary vortices.

To further accelerate vortex decay in ground proximity, differently shaped obstacles are imposed and the respective accelerated wake-vortex decay is quantified. The decay process is initiated nearly one t_0 earlier, whereas circulation levels relevant for aircraft separation are reached already two t_0 earlier. This rapid wake-vortex decay in ground proximity is achieved by the dedicated use of properties of vortex dynamics with the following characteristics.

1) Strong omega-shaped secondary vortices detach early.

2) Omega shaped secondary vortex approaches the primary vortex by self-induction.

3) After the secondary vortex has looped around the primary vortex, it separates and propagates along the primary vortex again driven by self-induction.

4) The dedicated secondary vortex remains connected to the regular ground effect vortex and thus obtains continued supply of energy.

5) The highly intense interaction of primary and secondary vortices leads to rapid wake-vortex decay independent from natural external disturbances.

These disturbances propagating along the wake vortices can also be considered as so-called end effects, where two different types are identified: one corresponding to a pressure disturbance inside the vortex core, and one corresponding to propagating helical vortex structures that develop from the rolled-up secondary vortices. The obstacles are optimized with respect to size and shape. It is shown that a plate line triggers even slightly higher decay rates than a much more massive block-shaped barrier. Headwind does not degrade the averaged circulation decay triggered by the plate line.

This purely numerical investigation was performed with wall-resolved LES at a relatively small Reynolds number. It is supposed that the presented effects of the obstacles, in particular the strong secondary vortex structures that trigger an early vortex decay, are relatively independent from the Reynolds number.

In summary, the introduction of plate lines at the ground supports the selective generation of secondary vortices and enables a smart utilization of vortex properties to generate fast approaching and rapidly spreading disturbances leading to early vortex decay in ground proximity. The installation of suitable obstacles at runway tails may improve safety by reducing the number of wake encounters and increase the efficiency of wake-vortex advisory systems. A respective patent entitled "Surface Structure on a Ground Surface for Accelerating Decay of Wake Turbulence in the Short Final of an Approach to a Runway" has been filed. A comparison with experiments performed in a water towing tank will also be presented. Flight experiments are planned at Oberpfaffenhofen Airport (Germany) to demonstrate the real-life functionality of plate lines for the initiation of early wake-vortex decay.

Acknowledgments

The simulations have been performed using supercomputers at Deutsches Klimarechenzentrum (DKRZ), Forschungszentrum Jülich and Leibniz-Rechenzentrum. We would like to thank Andreas Dörnbrack for providing computation time at DKRZ as well as M. Manhart for providing the original version of the large-eddy-simulation code MGLET. The work was funded by the DLR, German Aerospace Research Center project Wetter & Fliegen.

References

[1] Gerz, T., Holzäpfel, F., and Darracq, D., "Commercial Aircraft Wake Vortices," *Progress in Aerospace Sciences*, Vol. 38, No. 3, 2002,

pp. 181–208.
doi:10.1016/S0376-0421(02)00004-0

[2] Gerz, T., Holzäpfel, F., Bryant, W., Köpp, F., Ferch, M., Tafferner, A., and Winckelmans, G., "Research Towards a Wake-Vortex Advisory System for Optimal Aircraft Spacing," *Comptes Rendus Physique*, Vol. 6, Nos. 4–5, 2005, pp. 501–523.

[3] Spalart, P., "Airplane Trailing Vortices," *Annual Review of Fluid Mechanics*, Vol. 30, No. 1, 1998, pp. 107–138.
doi:10.1146/annurev.fluid.30.1.107

[4] Holzäpfel, F., and Steen, M., "Aircraft Wake-Vortex Evolution in Ground Proximity: Analysis and Parameterization," *AIAA Journal*, Vol. 45, No. 1, 2007, pp. 218–227.
doi:10.2514/1.23917

[5] Critchley, J., and Foot, P., "UK CAA Wake Vortex Database: Analysis of Incidents Reported Between 1982 and 1990," *Civil Aviation Authority*, Paper 91, London, 1991.

[6] Robins, R., and Delisi, D., "Potential Hazard of Aircraft Wake Vortices in Ground Effect with Crosswind," *Journal of Aircraft*, Vol. 30, No. 2, 1993, pp. 201–206.
doi:10.2514/3.48266

[7] Türk, L., Coors, D., and Jacob, D., "Behavior of Wake Vortices Near the Ground Over a Large Range of Reynolds Numbers," *Aerospace Science and Technology*, Vol. 3, No. 2, 1999, pp. 71–81.
doi:10.1016/S1270-9638(99)80031-5

[8] Harvey, J., and Perry, F., "Flowfield Produced by Trailing Vortices in the Vicinity of the Ground," *AIAA Journal*, Vol. 9, No. 8, 1971, pp. 1659–1660.
doi:10.2514/3.6415

[9] Dufresne, L., Baumann, R., Gerz, T., Winckelmans, G., Moet, H., and Capart, R., "Large Eddy Simulation of Wake Vortex Flows at Very High Reynolds Numbers: A Comparison of Different Methodologies," AWIATOR TR-D1.14-16, 2005.

[10] Spalart, P., Strelets, M., Travin, A., and Shur, M., "Modelling the Interaction of a Vortex Pair with the Ground," *Fluid Dynamics*, Vol. 36, No. 6, 2001, pp. 899–908.
doi:10.1023/A:1017958425271

[11] Proctor, F. H., Hamilton, D. W., and Han, J., "Wake Vortex Transport and Decay in Ground Effect: Vortex Linking with the Ground," *38th Aerospace Sciences Meeting and Exhibit*, AIAA Paper 2000-0757, Jan. 2000.

[12] Fabre, D., Jacquin, L., and Loof, A., "Optimal Perturbations in a Four-Vortex Aircraft Wake in Counter-Rotating Configuration," *Journal of Fluid Mechanics*, Vol. 451, Jan. 2002, pp. 319–328.
doi:10.1017/S0022112001006954

[13] Duponcheel, M., Lonfils, T., Bricteux, L., and Winckelmans, G., "Simulations of Three-Dimensional Wake Vortices in Ground Effect Using a Fourth-Order Incompressible Code," *Proceedings of the 7th National Congress on Theoretical and Applied Mechanics*, Mons, Belgium, 2006.

[14] Georges, L., Geuzaine, P., Duponchel, M., Bricteux, L., Lonfils, T., Winckelmans, G., and Giovannini, A., "LES of Two-Vortex System in Ground Effect with and Without Wind," Université Catholique de Louvain, Institut de Mécanique des Fluides de Toulouse TR-3.1.1-3, Belgium, 2005.

[15] Proctor, F. H., and Han, J., "Numerical Study of Wake Vortex Interaction with the Ground Using the Terminal Area Simulation System," *37th Aerospace Sciences Meeting and Exhibit*, AIAA Paper 1999-0754, Jan. 1999.

[16] Bao, F., and Vollmers, H., "Alleviation of End-Effects in Facilities for Far Wake Investigations," *43rd AIAA Aerospace Sciences Meeting and Exhibit*, AIAA Paper 2005-0907, 2005.

[17] Stephan, A., Holzäpfel, F., Misaka, T., Geisler, R., and Konrath, R., "Enhancement of Aircraft Wake Vortex Decay in Ground Proximity—Experiment Versus Simulation," *CEAS Bulletin* (to be published).

[18] Manhart, M., "A Zonal Grid Algorithm for DNS of Turbulent Boundary Layer," *Computer and Fluids*, Vol. 33, No. 3, 2004, pp. 435–461.
doi:10.1016/S0045-7930(03)00061-6

[19] Meneveau, C., Lund, T. S., and Cabot, W. H., "A Lagrangian Dynamic Subgrid-Scale Model of Turbulence," *Journal of Fluid Mechanics*, Vol. 319, July 1996, pp. 353–385.
doi:10.1017/S0022112096007379

[20] Hokpunna, A., and Manhart, M., "Compact Fourth-Order Finite Volume Method for Numerical Solutions of Navier–Stokes Equations on Staggered Grids," *Journal of Computational Physics*, Vol. 229, No. 20, 2010, pp. 7545–7570.
doi:10.1016/j.jcp.2010.05.042

[21] Holzäpfel, F., "Adjustment of Subgrid-Scale Parametrizations to Strong Streamline Curvature," *AIAA Journal*, Vol. 42, No. 7, 2004, pp. 1369–1377.
doi:10.2514/1.6076

[22] Delisi, D. P., Pruis, M. J., Wang, F. Y., and Lai, D. Y., "Estmates of the Initial Vortex Separation Distance, b_0, of Commercial Aircraft from Pulsed Lidar Data," *51st AIAA Aerospace Science Meeting*, AIAA Paper 2013-0365, 2013.

[23] Moser, R. D., Kim, J., and Mansour, N., "Direct Numerical Simulation of Turbulent Channel Flow up to $Re = 590$," *Physics of Fluids*, Vol. 11, No. 4, 1999, pp. 943–945.
doi:10.1063/1.869966

[24] Schlichting, H., and Gersten, G., *Grenzschicht-Theorie*, Springer, 1997, pp. 557–564.

[25] Jimenez, J., and Moin, P., "The Minimal Flow Unit in Near-Wall Turbulence," *Journal of Fluid Mechanics*, Vol. 225, April 1991, pp. 213–240.
doi:10.1017/S0022112091002033

[26] Grötzbach, G., "Direct Numerical and Large Eddy Simulations of Turbulent Channel Flows," *Encyclopedia of Fluid Mechanics*, edited by Cheremisinoff, N., Gulf Publishing Company, Houston, Texas, 1987, pp. 1337–1391.

[27] Lamb, H., *Hydrodynamics*, Cambridge Univ. Press, Cambridge, England, U.K., 1957, pp. 220–224.

[28] Saffman, P. G., "The Approach of a Vortex Pair to a Plane Surface in Inviscid Fluid," *Journal of Fluid Mechanics*, Vol. 92, No. 3, 1979, pp. 497–503.
doi:10.1017/S0022112079000744

[29] Doligalski, T. L., Smith, C., and Walker, J. D. A., "Vortex Interactions with Walls," *Annual Review of Fluid Mechanics*, Vol. 26, Jan. 1994, pp. 573–616.
doi:10.1146/annurev.fl.26.010194.003041

[30] Holzäpfel, F., Gerz, T., Frech, M., Tafferner, A., Köpp, F., Smalikho, I., Rahm, S., Hahn, K.-U., and Schwarz, C., "The Wake Vortex Prediction and Monitoring System WSVBS—Part 1: Design," *Air Traffic Control Quarterly*, Vol. 17, No. 4, 2009, pp. 301–322.

[31] Holzäpfel, F., "Probabilistic Two-Phase Wake Vortex Decay and Transport Model," *Journal of Aircraft*, Vol. 40, No. 2, 2003, pp. 323–331.
doi:10.2514/2.3096

[32] Steen, M., *Analyse und Parametrisierung des Wirbelschleppenverhaltens in Bodennähe*, M.S. Thesis, Technical Univ. of Brunswick, Brunswick, Germany, 2005.

[33] Holzäpfel, F., Gerz, T., and Baumann, R., "The Turbulent Decay of Trailing Vortex Pairs in Stably Stratified Environments," *Aerospace Science and Technology*, Vol. 5, No. 2, 2001, pp. 95–108.
doi:10.1016/S1270-9638(00)01090-7

[34] Misaka, T., Holzäpfel, F., Hennemann, I., Gerz, T., Manhart, M., and Schwertfirm, F., "Vortex Bursting and Tracer Transport of a Counter-Rotating Vortex Pair," *Physics of Fluids*, Vol. 24, No. 2, 2012, Paper 025104.
doi:10.1063/1.3684990

[35] Holzäpfel, F., Hofbauer, T., Darracq, D., Moet, H., Garnier, F., and Ferreira Gago, C., "Analysis of Wake Vortex Decay Mechanisms in the Atmosphere," *Aerospace Science and Technology*, Vol. 7, No. 4, 2003, pp. 263–275.
doi:10.1016/S1270-9638(03)00026-9

[36] Cantwell, B., Coles, D., and Dimotakis, P., "Structure and Entrainment in the Place of Symmetry of a Turbulent Spot," *Journal of Fluid Mechanics*, Vol. 87, No. 04, 1978, pp. 641–672.
doi:10.1017/S0022112078001809

[37] Butler, K. M., and Farrell, B. F., "Optimal Perturbations and Streak Spac-
ing in Wall Bounded Turbulent Shear Flow," *Physics of Fluids*, Vol. 5, 1993, pp. 774–777.
doi:10.1063/1.858663

[38] Ortega, J. M., Bristol, R. L., and Savas, Ö., "Experimental Study of the Instability of Unequal Strength Counter-Rotating Vortex Pairs," *Journal of Fluid Mechanics*, Vol. 474, Jan. 2003, pp. 35–84.
doi:10.1017/S0022112002002446

[39] Chapman, D. R., "Computational Aerodynamics Development and Outlook," *AIAA Journal*, Vol. 17, No. 12, 1979, pp. 1293–1313.
doi:10.2514/3.61311

[40] Moet, H., Laporte, F., Chevalier, G., and Poinsot, T., "Wave Propagation in Vortices and Vortex Bursting," *Physics of Fluids*, Vol. 17, 2005, Paper 054109.
doi:10.1063/1.1896937

[41] Stephan, A., Holzäpfel, F., and Misaka, T., "Aircraft Wake Vortex Decay in Ground Proximity—Physical Mechanisms and Artificial Enhancement," *4th AIAA Atmospheric and Space Environments Conference*, AIAA Paper 2012-2672, 2012.